

## ARTICLE

***In situ construction of BiOBr/Ag<sub>3</sub>PO<sub>4</sub> composites with enhanced visible light photocatalytic performances***Juntao Yan, Mengqiu Xu, Bo Chai,<sup>a)</sup> Haibo Wang, Chunlei Wang, and Zhandong Ren

School of Chemical and Environmental Engineering, Wuhan Polytechnic University, Wuhan 430023, People's Republic of China

(Received 3 December 2016; accepted 23 February 2017)

The BiOBr/Ag<sub>3</sub>PO<sub>4</sub> composites were fabricated by a facile *in situ* deposition of Ag<sub>3</sub>PO<sub>4</sub> nanoparticles on the BiOBr microsheets and analyzed by X-ray diffraction, scanning electron microscope, high resolution transmission electron microscope, X-ray photoelectron spectroscopy, UV-vis diffuse reflectance absorption spectra, Fourier transform infrared, Raman, photoluminescence (PL), and photoelectrochemical techniques. The photocatalytic performances of as-prepared samples were investigated and compared through degradation of Rhodamine B (RhB) solution. The results suggested that 30 wt% amount of BiOBr in the composites possessed the highest photocatalytic activity. The remarkably improved photocatalytic performances of BiOBr/Ag<sub>3</sub>PO<sub>4</sub> composites could be ascribed to the efficient separation of electron–hole pairs, due to suitable energy band potentials between BiOBr and Ag<sub>3</sub>PO<sub>4</sub>. Furthermore, the photoelectrochemical and PL tests verified the separation and transfer efficiency of charges was promoted.

**I. INTRODUCTION**

Solving the energy and environmental issues via semiconductor photocatalytic technology has attracted wide attention in the past decades.<sup>1,2</sup> Enormous efforts have been devoted to develop visible-light-induced photocatalysts such as BiOX (X = Cl, Br, I),<sup>3</sup> Bi<sub>2</sub>MoO<sub>6</sub>,<sup>4</sup> BiVO<sub>4</sub>,<sup>5</sup> Bi<sub>2</sub>WO<sub>6</sub>,<sup>6</sup> In<sub>2</sub>S<sub>3</sub>,<sup>7</sup> ZnIn<sub>2</sub>S<sub>4</sub>,<sup>8</sup> AgBr,<sup>9</sup> Ag<sub>3</sub>PO<sub>4</sub>,<sup>10</sup> Ag<sub>2</sub>CO<sub>3</sub>,<sup>11</sup> AgVO<sub>3</sub>,<sup>12</sup> and g-C<sub>3</sub>N<sub>4</sub>,<sup>13</sup> considering full harvesting of solar light. Among these catalysts, Ag<sub>3</sub>PO<sub>4</sub> has been seemed as a very promising candidate for photocatalytic applications because of its good photodegradation organic dyes capacity. However, bare Ag<sub>3</sub>PO<sub>4</sub> is prone to photocorrosion and decomposing to low active Ag in the process of photoreaction, which could seriously deteriorate its photocatalytic activity.<sup>14</sup> To solve this problem and improve stability, coupling Ag<sub>3</sub>PO<sub>4</sub> with other semiconductors to formation composites has been extensively developed, for instance, Ag<sub>3</sub>PO<sub>4</sub>/TiO<sub>2</sub>,<sup>15</sup> Ag<sub>3</sub>PO<sub>4</sub>/ZnO,<sup>16</sup> Ag<sub>3</sub>PO<sub>4</sub>/SnO<sub>2</sub>,<sup>17</sup> Ag<sub>3</sub>PO<sub>4</sub>/Bi<sub>2</sub>MoO<sub>6</sub>,<sup>18</sup> Ag<sub>3</sub>PO<sub>4</sub>/Bi<sub>2</sub>WO<sub>6</sub>,<sup>19</sup> Ag<sub>3</sub>PO<sub>4</sub>/WO<sub>3</sub>,<sup>20</sup> Ag<sub>3</sub>PO<sub>4</sub>/g-C<sub>3</sub>N<sub>4</sub>,<sup>21</sup> Ag<sub>3</sub>PO<sub>4</sub>/BiVO<sub>4</sub>,<sup>22</sup> and so on. The well-matched energy bands' structure of these composites is beneficial for the separation and migration of electron–hole pairs and then boosting the photoactivity and photostability.

The layered structure of BiOX (X = Cl, Br, I) gives high carrier mobility and little recombination of electron–hole pairs, which make it become an excellent photocatalyst.

However, the photocatalytic performance of BiOX should be further improved from the practical applications. Until now, a large number of BiOX-based composites such as BiOCl/g-C<sub>3</sub>N<sub>4</sub>,<sup>23</sup> BiOI/TiO<sub>2</sub>,<sup>24</sup> BiOI/Bi<sub>2</sub>WO<sub>6</sub>,<sup>25</sup> BiOBr/ZnFe<sub>2</sub>O<sub>4</sub>,<sup>26</sup> BiOBr/Bi<sub>2</sub>WO<sub>6</sub>,<sup>27</sup> BiOBr/BiVO<sub>4</sub>,<sup>28</sup> BiOBr/BiMoO<sub>6</sub>,<sup>29</sup> and BiOBr/g-C<sub>3</sub>N<sub>4</sub><sup>30</sup> have been reported, which exhibit the improved photocatalytic activity than that of single BiOX. Recently some research groups have combined BiOX with Ag<sub>3</sub>PO<sub>4</sub> to fabricate BiOX/Ag<sub>3</sub>PO<sub>4</sub> composites. The resultant photocatalysts (BiOCl/Ag<sub>3</sub>PO<sub>4</sub>,<sup>31</sup> BiOBr/Ag<sub>3</sub>PO<sub>4</sub>,<sup>32</sup> BiOI/Ag<sub>3</sub>PO<sub>4</sub><sup>33,34</sup>) display the outstanding photoactivity and photostability. Based on the aforesaid reports, construction of BiOX/Ag<sub>3</sub>PO<sub>4</sub> composites is a practicable and convenient approach to improve the photocatalytic performances of Ag<sub>3</sub>PO<sub>4</sub> and BiOX.

In this work, BiOBr/Ag<sub>3</sub>PO<sub>4</sub> composites were synthesized by a convenient *in situ* deposition of Ag<sub>3</sub>PO<sub>4</sub> nanoparticles on BiOBr microsheets and applied into photocatalytic degradation of RhB solution under visible light illumination. Remarkably improved photocatalytic performance was realized in comparison with single BiOBr and Ag<sub>3</sub>PO<sub>4</sub>. In addition, the effect of composition ratio on photocatalytic activity was investigated.

**II. EXPERIMENTAL SECTION****A. Materials preparation**

BiOBr microsheets were synthesized according to the previous report.<sup>35</sup> Briefly, 0.970 g Bi(NO<sub>3</sub>)<sub>3</sub>·5H<sub>2</sub>O was added into 3 mL acetic acid (HAc) to form a transparent solution. The solution was mixed with 30 mL deionized

Contributing Editor: Xiaobo Chen

<sup>a)</sup>Address all correspondence to this author.

e-mail: willycb@163.com

DOI: 10.1557/jmr.2017.89

water including 0.240 g KBr by magnetic stirring for 30 min. After that, the mixture was transferred into a 50 mL Teflon-lined stainless steel autoclave and heated at 160 °C for 6 h. After being cooled to room temperature, the products were obtained by centrifugation, washed with deionized water and ethanol for three times, and then dried at 80 °C for 12 h.

For the fabrication of BiOBr/Ag<sub>3</sub>PO<sub>4</sub> composites, the appropriate amount of BiOBr was ultrasonically dispersed into 30 mL deionized water for 30 min. Then 0.170 g AgNO<sub>3</sub> was added into the BiOBr suspension. The pH value of mixture was changed to 7.00 by dilute ammonium hydroxide. After stirring another 30 min, 20 mL deionized water containing 0.127 g Na<sub>3</sub>PO<sub>4</sub>·12H<sub>2</sub>O was introduced into the above mixture. Subsequently, the mixture was stirred for 4 h in the dark at ambient temperature. Then, the wet powders were collected, centrifuged, washed with ethanol and deionized water, and dried at 60 °C for 6 h. According to this procedure, different theoretical weight ratios of BiOBr/Ag<sub>3</sub>PO<sub>4</sub> samples from 10 wt% to 70 wt% BiOBr in the composites were synthesized through tuning the BiOBr amounts. For comparison, the bare Ag<sub>3</sub>PO<sub>4</sub> was also fabricated in terms of the same steps except the addition of BiOBr.

## B. Material characterization

X-ray diffraction (XRD) was performed by a Bruker D8 Advance X-ray diffractometer (Bruker Corporation, Karlsruhe, Germany) with Cu K $\alpha$  irradiation ( $\lambda = 0.154178$  nm). The morphology of samples was conducted by Hitachi S-3000N scanning electron microscope (SEM; Hitachi Co. Ltd., Tokyo, Japan) and JEM 2100F high resolution transmission electron microscope (HRTEM; JEOL Ltd., Tokyo, Japan). The X-ray photoelectron spectroscopy (XPS) test was recorded on a VG Multilab 2000 (Thermo Fisher Scientific, Waltham, Massachusetts) with Al K $\alpha$  source. The Fourier transform infrared (FTIR) spectra of samples were carried out using a Thermo Nicolet Avatar 360 spectrometer (Thermo Fisher Scientific). Raman spectra were examined by a Renishaw RM-1000 spectrometer (Renishaw plc, Gloucestershire, United Kingdom). The UV-vis diffuse reflectance absorption spectra (UV-DRS) were monitored on a Purkinje General TU-1901 spectrophotometer. The photoluminescence spectra (PL) were measured using a Varian Cary Eclipse fluorescence spectrophotometer (Varian, Palo Alto, California).

## C. Photocatalytic degradation

The photocatalytic activities of BiOBr/Ag<sub>3</sub>PO<sub>4</sub> composites were evaluated by the degradation of Rhodamine B (RhB) solution under visible light irradiation using a 500 W xenon lamp (Changzhou Yuyu Electro-Optical Device Co. Ltd, Changzhou, China) as a light source with a 420 nm cut-off filter. In each experiment,

50 mg of catalyst was added in 100 mL of RhB aqueous solution ( $1.0 \times 10^{-5}$  mol/L). Before illumination, the suspensions were stirred in the dark for 30 min to establish the adsorption–desorption balance. At 5 min intervals, about 4 mL suspensions was collected and centrifuged at 10,000 rpm for 10 min to remove the catalyst. The concentration of RhB was determined by measuring the UV–vis spectra of the maximum absorption wavelength using a TU-1810 spectrophotometer.

## D. Photoelectrochemical measurement

The electrochemical impedance spectroscopy (EIS) measurement was carried out using an electrochemical system (CHI 760D, CH Instruments Co. Ltd., Shanghai, China) in a three-electrode cell constituted of the working electrode, a platinum foil as the counter electrode, a Ag/AgCl electrode as the reference electrode, and 0.1 mol/L Na<sub>2</sub>SO<sub>4</sub> solution as the electrolyte. For the preparation of working electrodes, 20 mg of as-prepared catalysts was ultrasonically dispersed in a mixture solution of 1 mL ethanol and 0.1 mL nafion aqueous solution (5 wt%) for 30 min. After that, 0.1 mL suspension was spread on an indium tin oxide (ITO) glass with a fixed area of 1 cm<sup>2</sup> and dried in air at ambient temperature.

## III. RESULTS AND DISCUSSION

Figure 1 shows the XRD of BiOBr, Ag<sub>3</sub>PO<sub>4</sub> and 30 wt% BiOBr/Ag<sub>3</sub>PO<sub>4</sub> composite. From the BiOBr diffraction pattern, all the detectable peaks could be assigned to the tetragonal phase BiOBr (JCPDS NO. 73-2061) with well resolvable (001), (002), (011), (012), (110), (003), (112), (004), (014), (114), and (212) reflections, in consistent with the previous report.<sup>35</sup> It is noteworthy that the intensities of (001), (002), (003), and (004) crystal planes obviously increase comparing with the standard card, implying that the

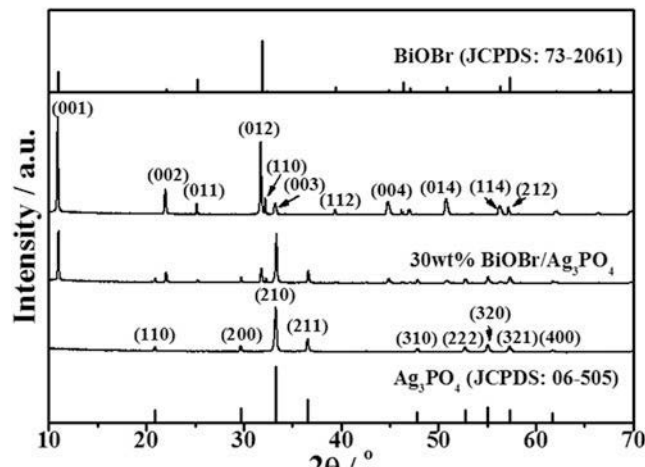


FIG. 1. XRD patterns of BiOBr, Ag<sub>3</sub>PO<sub>4</sub> and 30 wt% BiOBr/Ag<sub>3</sub>PO<sub>4</sub> composite.

BiOBr products preferentially grow along the (001) plane. The characteristic peaks of pristine Ag<sub>3</sub>PO<sub>4</sub> could well correspond to the cubic phase of Ag<sub>3</sub>PO<sub>4</sub> (JCPDS, No. 06–505).<sup>10</sup> As for the 30 wt% BiOBr/Ag<sub>3</sub>PO<sub>4</sub> composite, it presents the coexistence of BiOBr and Ag<sub>3</sub>PO<sub>4</sub> crystal phases. No impurity phases of Ag, AgBr, or BiPO<sub>4</sub> occur in the BiOBr/Ag<sub>3</sub>PO<sub>4</sub> composite. In addition, the diffraction peak intensities of BiOBr distinctly fade away, which could be due to the Ag<sub>3</sub>PO<sub>4</sub> nanoparticles tightly enwrapping the surface of BiOBr, then decreasing the diffraction peak intensities of BiOBr.

Figures 2(a)–2(d) reveals the SEM images of BiOBr, Ag<sub>3</sub>PO<sub>4</sub> and 30 wt% BiOBr/Ag<sub>3</sub>PO<sub>4</sub> composite. The single BiOBr shows the evident two-dimensional (2D) sheet-like structure with the diameter of 1–3 μm and thickness of 50–100 nm, in agreement with the previous report.<sup>35</sup> Pure Ag<sub>3</sub>PO<sub>4</sub> exhibits irregular nanoparticle-like morphology with the diameter of 50–100 nm. As for the 30 wt% BiOBr/Ag<sub>3</sub>PO<sub>4</sub> composite, it is composed of the micro-sheets and nanoparticles, which are respectively ascribed to BiOBr and Ag<sub>3</sub>PO<sub>4</sub>. Moreover, these granular Ag<sub>3</sub>PO<sub>4</sub> are mainly attached on the surface of BiOBr microsheets. The microstructure of 30 wt% BiOBr/Ag<sub>3</sub>PO<sub>4</sub> composite is investigated by HRTEM observations. Figure 2(e) identifies that the Ag<sub>3</sub>PO<sub>4</sub> nanoparticles are intimately adhered on the surface of BiOBr, in accordance with the SEM measurement. In Fig. 2(f), the interplanar spacings of lattice fringes are determined to be 0.230 and 0.270 nm,

assigning to the (112) plane of BiOBr and the (210) plane of Ag<sub>3</sub>PO<sub>4</sub>, respectively.

To further detect the chemical composition and valence state of various ingredients, the 30 wt% BiOBr/Ag<sub>3</sub>PO<sub>4</sub> composite was characterized by XPS. From the XPS survey spectrum [Fig. 3(a)], the composite is consisted of Bi, Ag, Br, P, and O elements. Two strong peaks at about 159.3 and 164.6 eV in Fig. 3(b) are respectively attributed to Bi 4f<sub>7/2</sub> and Bi 4f<sub>5/2</sub>, indicating that Bi<sup>3+</sup> exists in the composites.<sup>36</sup> In the high-resolution Ag 3d XPS spectrum [Fig. 3(c)], the peaks with binding energies of 367.8 and 373.7 eV were attributed to Ag 3d<sub>5/2</sub> and Ag 3d<sub>3/2</sub>, implying that Ag<sup>+</sup> is existence in the composite.<sup>16</sup> The Br 3d XPS spectrum [Fig. 3(d)] could be fitted as two peaks, and the binding energies at 68.7 and 69.7 eV are assigned with Br 3d<sub>5/2</sub> and Br 3d<sub>3/2</sub>.<sup>36</sup> The P 2p XPS peak is found at 132.5 eV [Fig. 3(e)], which could be related to P<sup>5+</sup> in the Ag<sub>3</sub>PO<sub>4</sub>.<sup>20</sup> As for the O 1s XPS spectrum [Fig. 3(f)], it could be deconvoluted into three peaks at 530.1, 530.7, and 532.0 eV, corresponding to the Bi–O bonds of BiOBr, the PO<sub>4</sub><sup>3-</sup> bonds of Ag<sub>3</sub>PO<sub>4</sub>, and the O–H bonds, respectively. The XPS results illustrate that the composites are constructed with the BiOBr and Ag<sub>3</sub>PO<sub>4</sub>.

Figure 4(a) depicts the FTIR spectra of BiOBr, Ag<sub>3</sub>PO<sub>4</sub> and 30 wt% BiOBr/Ag<sub>3</sub>PO<sub>4</sub> composite. The peaks at 3430 and 1660 cm<sup>-1</sup> are respectively attributed to the vibration mode of –OH groups derived from the adsorbed H<sub>2</sub>O molecules.<sup>22</sup> As for bare BiOBr, the featured peak existing

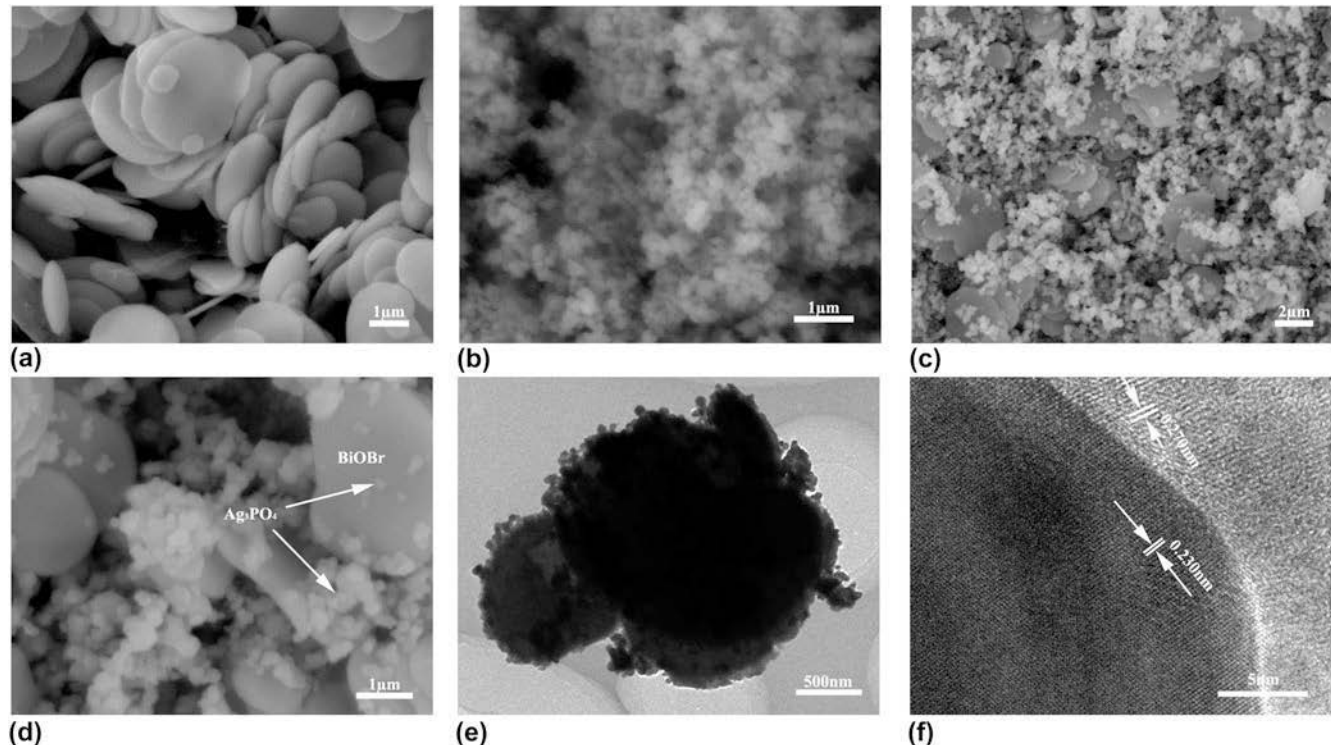


FIG. 2. SEM images of BiOBr (a) and Ag<sub>3</sub>PO<sub>4</sub> (b); low magnification (c) and high magnification (d) SEM images of 30 wt% BiOBr/Ag<sub>3</sub>PO<sub>4</sub> composite; TEM (e) and HRTEM (f) images of 30 wt% BiOBr/Ag<sub>3</sub>PO<sub>4</sub> composite.

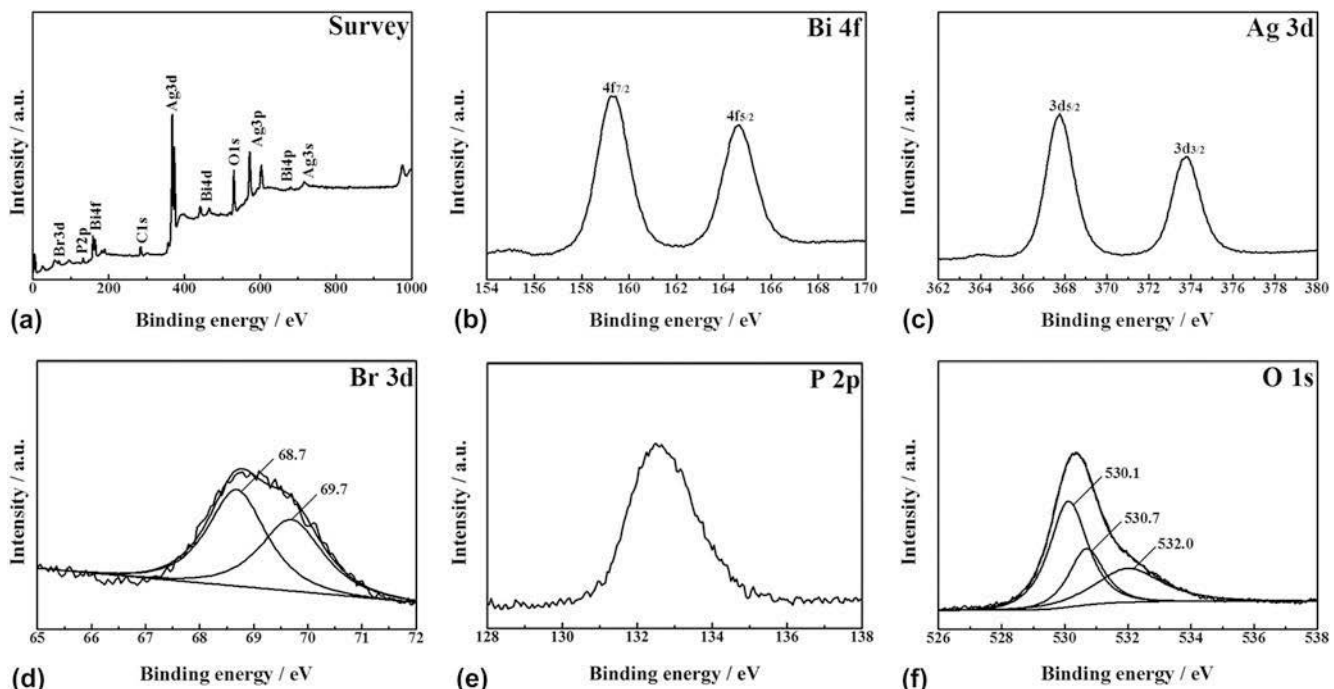


FIG. 3. XPS spectra of 30 wt% BiOBr/Ag<sub>3</sub>PO<sub>4</sub> composite: (a) XPS survey spectrum; (b) high resolution Bi 4f spectrum; (c) high resolution Ag 3d spectrum; (d) high resolution Br 3d spectrum; (e) high resolution P 2p spectrum; (f) high resolution O 1s spectrum.

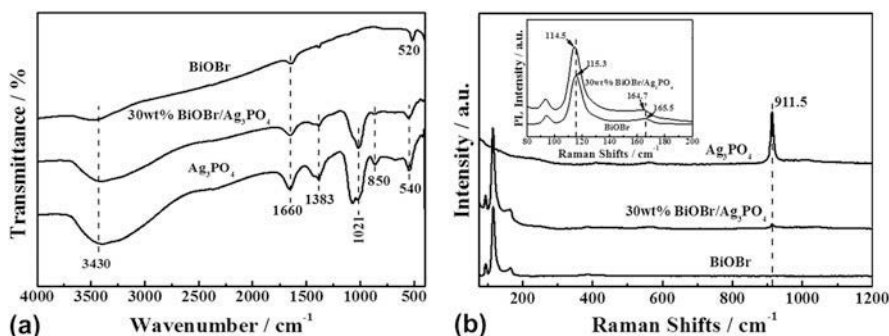


FIG. 4. FTIR (a) and Raman (b) spectra of BiOBr, Ag<sub>3</sub>PO<sub>4</sub> and 30 wt% BiOBr/Ag<sub>3</sub>PO<sub>4</sub> composite, the partial magnification Raman curves (inset).

at 520 cm<sup>-1</sup> is related to Bi–O vibration.<sup>32</sup> In the case of Ag<sub>3</sub>PO<sub>4</sub>, the peak centered at 540 cm<sup>-1</sup> is due to O = P–O bonds bending vibration. The absorption peaks around 850 and 1021 cm<sup>-1</sup> are assigned to the symmetric and asymmetric vibration of P–O–P bonds. The peak at 1383 cm<sup>-1</sup> originates from the P = O bonds vibration.<sup>22</sup> The FTIR spectrum of 30 wt% BiOBr/Ag<sub>3</sub>PO<sub>4</sub> composite substantially remains the characteristic absorption peaks of Ag<sub>3</sub>PO<sub>4</sub>. The vibration peaks ascribing to BiOBr are not distinct due to the relatively weak absorption or approaching to the O = P–O bond bending vibration of Ag<sub>3</sub>PO<sub>4</sub>.

Figure 4(b) shows a comparison of the Raman spectra of BiOBr, Ag<sub>3</sub>PO<sub>4</sub> and 30 wt% BiOBr/Ag<sub>3</sub>PO<sub>4</sub> composite. As far as BiOBr, the strong peaks at 115.3 and 165.5 cm<sup>-1</sup> (inset) could be attributed to the A<sub>1g</sub> and E<sub>g</sub> internal Bi–Br stretching modes, respectively.<sup>37</sup> For Ag<sub>3</sub>PO<sub>4</sub>, the peak at

911.5 cm<sup>-1</sup> is ascribed to the PO<sub>4</sub><sup>3-</sup> vibration.<sup>21</sup> In terms of the 30 wt% BiOBr/Ag<sub>3</sub>PO<sub>4</sub> composite, all the Raman bands belonging to BiOBr and Ag<sub>3</sub>PO<sub>4</sub> can be observed. Furthermore, the characteristic peaks assigning to the Bi–Br stretching mode have the slight shifts from 115.3 to 114.5 cm<sup>-1</sup> and from 165.5 to 164.7 cm<sup>-1</sup>, implying the interaction existence between BiOBr and Ag<sub>3</sub>PO<sub>4</sub>.

Figure 5 exhibits UV-DRS spectra of BiOBr, Ag<sub>3</sub>PO<sub>4</sub> and 30 wt% BiOBr/Ag<sub>3</sub>PO<sub>4</sub> composite. As shown, BiOBr presents an absorption edge at 435 nm, while Ag<sub>3</sub>PO<sub>4</sub> is 506 nm. According to the equation of  $E_g = 1240/\lambda_g$ , the band gap energies of BiOBr and Ag<sub>3</sub>PO<sub>4</sub> are respectively calculated to be 2.85 and 2.45 eV, where  $E_g$  is the band gap energy and  $\lambda_g$  is the absorption edge. The 30 wt% BiOBr/Ag<sub>3</sub>PO<sub>4</sub> composite reveals a combination of the two UV-DRS spectra.

The photocatalytic activities of as-prepared samples were evaluated by the photocatalytic degradation of RhB solution. The control experiments and physical mixed sample were carried out in the same photocatalytic reaction. As shown in Fig. 6(a), the RhB molecules are hardly degraded after 30 min visible light illumination without catalysts. Single Ag<sub>3</sub>PO<sub>4</sub> exhibits poor adsorption capacity. During 30 min visible light irradiation, the decolorization percentage of RhB is 16.8%. Pristine BiOBr shows the highest adsorption activity, and the decrease

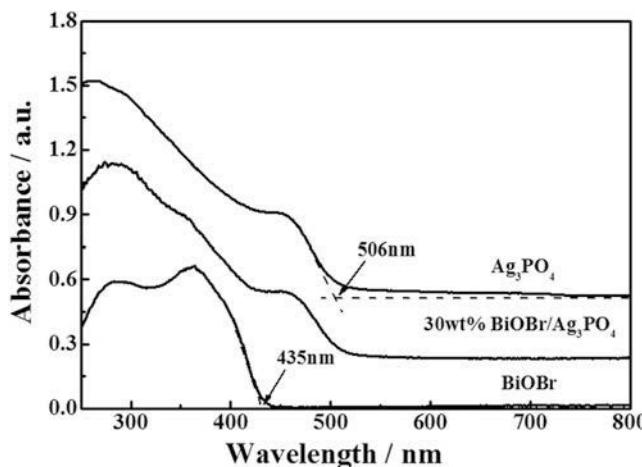


FIG. 5. UV-vis diffuse reflectance absorption spectra of BiOBr, Ag<sub>3</sub>PO<sub>4</sub> and 30 wt% BiOBr/Ag<sub>3</sub>PO<sub>4</sub> composite.

of RhB concentration achieving 36.1% after visible light irradiation for 30 min. The adsorption abilities of BiOBr/Ag<sub>3</sub>PO<sub>4</sub> composites enhance slightly along with increasing the amount of BiOBr in the composites. The decolorization percentages of RhB molecules are about 38.3%, 87.9%, 99.0%, 81.1%, and 68.8% for the 10 wt%, 20 wt%, 30 wt%, 50 wt%, and 70 wt% BiOBr/Ag<sub>3</sub>PO<sub>4</sub> composites after 30 min visible light illumination, respectively. It is obvious that the photocatalytic activities improve with increasing the BiOBr contents in the composites and the 30 wt% BiOBr/Ag<sub>3</sub>PO<sub>4</sub> composite manifests the best photocatalytic performance. Whereas further enhancing BiOBr amounts, the photocatalytic activities decline because the excessive BiOBr in the composites leads to the interfacial contact decrease between BiOBr and Ag<sub>3</sub>PO<sub>4</sub>. As for the physical mixed sample (30 wt% BiOBr and 70 wt% Ag<sub>3</sub>PO<sub>4</sub>), after 30 min visible light irradiation, the decolorization percentage of RhB is about 74.0%, which is lower than that of *in situ* prepared 30 wt% BiOBr/Ag<sub>3</sub>PO<sub>4</sub> composite. The results indicate that it is important to construct intimate contact between BiOBr and Ag<sub>3</sub>PO<sub>4</sub> for the improvement of photocatalytic activity. The temporal UV-visible absorption spectral variations of RhB solution over Ag<sub>3</sub>PO<sub>4</sub>, 30 wt% BiOBr/Ag<sub>3</sub>PO<sub>4</sub> and BiOBr samples are illustrated in Figs. 6(b)–6(d), respectively. It is evident that the construction of BiOBr/Ag<sub>3</sub>PO<sub>4</sub> composites could markedly boost the photocatalytic activity. It is also found that the maximal absorbance ( $\lambda_{\max}$ ) has slightly

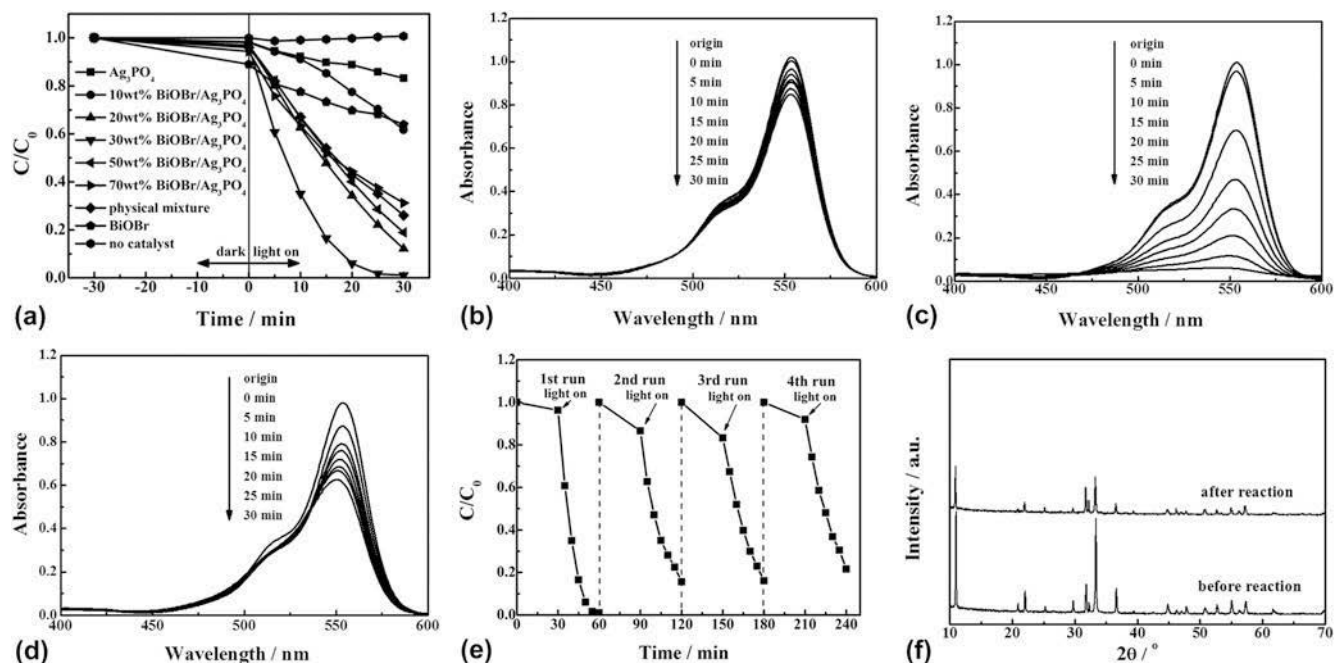


FIG. 6. Comparison of photocatalytic activities of different samples for the degradation of RhB solution (a); the temporal UV-vis absorption spectra during the photocatalytic degradation of RhB mediated by Ag<sub>3</sub>PO<sub>4</sub> (b), 30 wt% BiOBr/Ag<sub>3</sub>PO<sub>4</sub> (c), and BiOBr (d), “origin” means the concentration of RhB before absorption equilibrium; recycling photocatalytic degradation of RhB solution (e) and XRD patterns (f) of 30 wt% BiOBr/Ag<sub>3</sub>PO<sub>4</sub> composite before and after photocatalytic reaction.

blue shift in the BiOBr sample during visible light illumination, indicating that degradation of RhB molecules is a stepwise removal of the *N*-ethyl groups over BiOBr photocatalyst.

To study the stability of photocatalysts, the 30 wt% BiOBr/Ag<sub>3</sub>PO<sub>4</sub> composite was reused under the same conditions, as shown in Fig. 6(e). It is clear that the photocatalytic performance has mild reduction after the first run visible light irradiation. However, the photocatalytic efficiency still has 78.5% after four runs of degradation of RhB. The crystalline structures of the recycled 30 wt% BiOBr/Ag<sub>3</sub>PO<sub>4</sub> composite were also investigated, as shown in Fig. 6(f). It can be seen that there are no extra characteristic diffraction peaks in the XRD patterns. The moderate decrease of the diffraction peak intensities indicates the declined crystallinity after photocatalytic reaction. It suggests that the slight photocorrosion has happened.

To clarify the reaction mechanism, 10 mmol/L triethanolamine (TEOA), 10 mmol/L *p*-benzoquinone (BQ), and 1 mmol/L isopropanol (IPA) were respectively added into the photocatalytic reaction system as the scavengers of holes ( $h^+$ ), superoxide radicals ( $\cdot O_2^-$ ), and hydroxyl radicals ( $\cdot OH$ ) to investigate the effects of reactive species on photocatalytic degradation of RhB. As shown in Fig. 7(a), the TEOA and BQ lead to the dramatically inhibition of the degradation efficiency of RhB. However, IPA showed a weak constraint on degradation efficiency. The results reveal that  $h^+$  and  $\cdot O_2^-$  make the crucial roles in the degradation of RhB.

As we all know that the efficient charge separation and transfer is significant for the improvement of photocatalytic activity. The EIS spectra have been used to study the interfacial charge separation efficiency. From Fig. 7(b), the diameter of Nyquist circle of 30 wt% BiOBr/Ag<sub>3</sub>PO<sub>4</sub> composite is shorter than those of pure Ag<sub>3</sub>PO<sub>4</sub> and BiOBr samples, which means an effective interfacial charge transfer and separation. This result suggests that coupling Ag<sub>3</sub>PO<sub>4</sub> with BiOBr to formation composites is beneficial for the enhancement of photocatalytic activity.

To further illustrate the effective separation of photo-generated charge carriers in the BiOBr/Ag<sub>3</sub>PO<sub>4</sub> composites, the PL spectra measurements were performed at room temperature. Generally, the lower PL intensity, the smaller probability of photogenerated charge carriers recombination. In Fig. 7(c), the PL intensity of 30 wt% BiOBr/Ag<sub>3</sub>PO<sub>4</sub> composite is distinctly weakened, indicating that the recombination of photogenerated charge carriers is greatly restrained. The result also confirms that the BiOBr/Ag<sub>3</sub>PO<sub>4</sub> composite could effectively separate photogenerated electron–hole pairs.

Based on the aforementioned experimental results, a possible mechanism is proposed to explicate the improvement of photocatalytic activity of BiOBr/Ag<sub>3</sub>PO<sub>4</sub> composite. As for the semiconductor composites, the band edge potentials make a significant role in determining the flowchart of photogenerated electron–hole pairs. The potentials of the conduction band (CB) and valence band (VB) edge potentials of Ag<sub>3</sub>PO<sub>4</sub> and BiOBr are calculated by Mulliken electronegativity theory

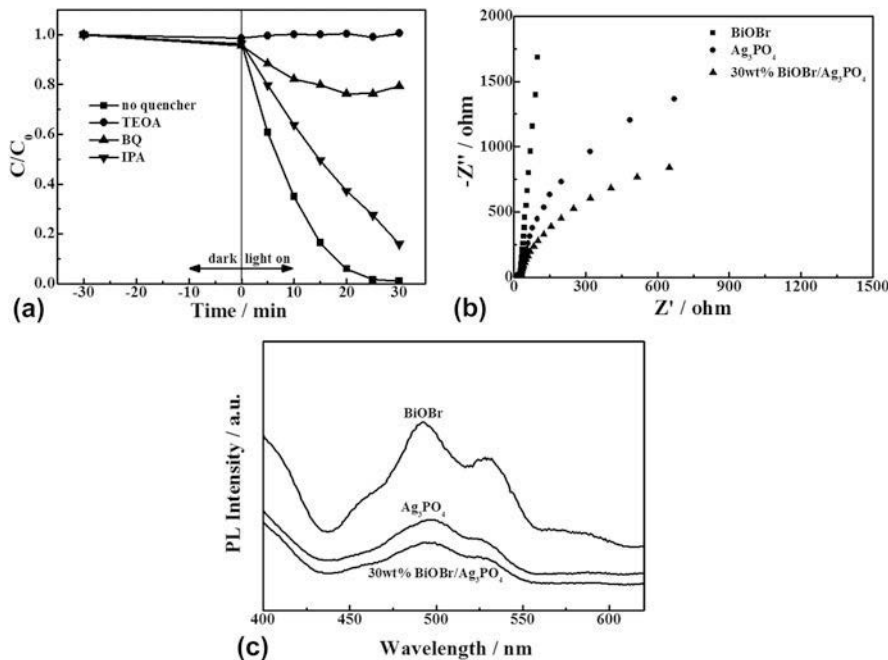


FIG. 7. The effect of reactive species on the photocatalytic degradation of RhB solution over the 30 wt% BiOBr/Ag<sub>3</sub>PO<sub>4</sub> composite (a); electrochemical impedance spectra Nyquist plots (b) and PL emission spectra (c) of BiOBr, Ag<sub>3</sub>PO<sub>4</sub> and 30 wt% BiOBr/Ag<sub>3</sub>PO<sub>4</sub> composite.

$E_{VB} = X - E_e + 0.5 E_g$ , where  $E_{VB}$  is the VB edge potential,  $X$  is the electronegativity of semiconductor, which can be expressed as the geometric mean of the absolute electronegativity of constituent atoms.<sup>27</sup> The  $X$  values of Ag<sub>3</sub>PO<sub>4</sub> and BiOBr are calculated to be 5.97 and 6.20 eV, respectively.  $E_e$  is the energy of free electrons on the hydrogen scale (approximately –4.5 eV). The  $E_g$  values of Ag<sub>3</sub>PO<sub>4</sub> and BiOBr are about 2.45 and 2.85 eV from the UV-DRS measurements, respectively. The  $E_{VB}$  of Ag<sub>3</sub>PO<sub>4</sub> and BiOBr are calculated to be 2.69 and 3.12 eV, respectively. The conduction band edge potential ( $E_{CB}$ ) can be acquired by the formula,  $E_{CB} = E_{VB} - E_g$ . Accordingly, the  $E_{CB}$  of Ag<sub>3</sub>PO<sub>4</sub> and BiOBr are estimated to be 0.24 and 0.27 eV, respectively. As shown in Fig. 8, when the BiOBr/Ag<sub>3</sub>PO<sub>4</sub> composite is illuminated under visible light, both Ag<sub>3</sub>PO<sub>4</sub> and BiOBr can be excited to generate electron–hole pairs. The electrons in the CB of Ag<sub>3</sub>PO<sub>4</sub> can transfer into the CB of BiOBr; meanwhile, the holes in the VB of BiOBr can conveniently migrate into the VB of Ag<sub>3</sub>PO<sub>4</sub>. As a result, the electron–hole pairs are efficiently separated between Ag<sub>3</sub>PO<sub>4</sub> and BiOBr; the recombination of electron–hole pairs can be prevented, in agreement with the results of PL and EIS tests. Since the CB potential of BiOBr and Ag<sub>3</sub>PO<sub>4</sub> is more positive than the single electron reduction potential of O<sub>2</sub>/O<sub>2</sub><sup>–</sup> (–0.046 eV vs. NHE),<sup>18</sup> it could not reduce O<sub>2</sub> to yield ·O<sub>2</sub><sup>–</sup> on the surfaces of BiOBr and Ag<sub>3</sub>PO<sub>4</sub>. However, the redox potentials of RhB and RhB\* are 0.95 and –1.42 eV (vs. NHE), respectively.<sup>38</sup> Because of the good adsorption capacity of BiOBr, the excited RhB\* molecules can inject the electrons into the CB of BiOBr, then reducing the surface chemisorbed O<sub>2</sub> to give ·O<sub>2</sub><sup>–</sup> via one electron reaction. The VB potential of Ag<sub>3</sub>PO<sub>4</sub> is not more positive than the redox potentials of ·OH/H<sub>2</sub>O (2.72 eV vs. NHE). It implies that the photogenerated h<sup>+</sup> in the VB of Ag<sub>3</sub>PO<sub>4</sub> could not react with H<sub>2</sub>O to form ·OH. Meanwhile, the production of ·OH

on BiOBr is almost impossible because the standard redox potential of Bi<sup>V</sup>/Bi<sup>III</sup> (1.59 eV vs. NHE) is more negative than that of ·OH/H<sub>2</sub>O.<sup>35</sup> In view of this, the photogenerated holes directly oxidize the RhB molecules in the reaction process.

#### IV. CONCLUSIONS

The BiOBr/Ag<sub>3</sub>PO<sub>4</sub> composites have been synthesized via a facile *in situ* deposition of Ag<sub>3</sub>PO<sub>4</sub> nanoparticles on BiOBr microsheets and applied into the photocatalytic degradation of RhB solution. The improved photocatalytic activity is achieved over the BiOBr/Ag<sub>3</sub>PO<sub>4</sub> composites in comparison with the single BiOBr and Ag<sub>3</sub>PO<sub>4</sub>, which could be attributed to the effective separation and migration of photogenerated electron–hole pairs. PL and EIS measurements demonstrate the efficient separation of photogenerated charge carriers in the BiOBr/Ag<sub>3</sub>PO<sub>4</sub> composites. Additionally, the measurements of radical scavengers suggest that h<sup>+</sup> and ·O<sub>2</sub><sup>–</sup> are the main active species for the degradation of RhB in the current system. The resultant BiOBr/Ag<sub>3</sub>PO<sub>4</sub> composites may have a broad application prospect in the pollutant removal as the highly efficient photocatalysts.

#### ACKNOWLEDGMENTS

This work was supported by the National Natural Science Foundation of China (No. 51302200), Scientific and Technological Support Project of Hubei Province (No. 2015BAA100), Research and Innovation Initiatives of Wuhan Polytechnic University (Nos. 2016y18 and 2015d4).

#### REFERENCES

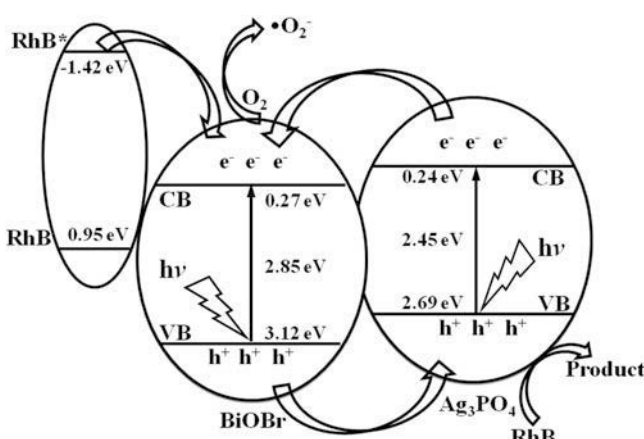


FIG. 8. The proposed mechanism of enhanced photocatalytic activity for the BiOBr/Ag<sub>3</sub>PO<sub>4</sub> composite.

1. D.N. Chen, X.G. Zhang, and A.F. Lee: Synthetic strategies to nanostructured photocatalysts for CO<sub>2</sub> reduction to solar fuels and chemicals. *J. Mater. Chem. A* **3**, 14487 (2015).
2. X.X. Zou and Y. Zhang: Noble metal-free hydrogen evolution catalysts for water splitting. *Chem. Soc. Rev.* **44**, 5148 (2015).
3. X.F. Chang, J. Huang, C. Cheng, Q. Sui, W. Sha, G.B. Ji, S.B. Deng, and G. Yu: BiOX (X = Cl, Br, I) photocatalysts prepared using NaBiO<sub>3</sub> as the Bi source: Characterization and catalytic performance. *Catal. Commun.* **11**, 460 (2010).
4. L.W. Zhang, T.G. Xu, X. Zhao, and Y.F. Zhu: Controllable synthesis of Bi<sub>2</sub>MoO<sub>6</sub> and effect of morphology and variation in local structure on photocatalytic activities. *Appl. Catal., B* **98**, 138 (2010).
5. M. Ou, H.Y. Nie, Q. Zhong, S.L. Zhang, and L. Zhong: Controllable synthesis of 3D BiVO<sub>4</sub> superstructures with visible-light-induced photocatalytic oxidation of NO in the gas phase and mechanistic analysis. *Phys. Chem. Chem. Phys.* **17**, 28809 (2015).
6. L.W. Zhang and Y.F. Zhu: A review of controllable synthesis and enhancement of performances of bismuth tungstate visible-light-driven photocatalysts. *Catal. Sci. Technol.* **2**, 694 (2012).
7. J. Chen, W.X. Liu, and W.W. Gao: Tuning photocatalytic activity of In<sub>2</sub>S<sub>3</sub> broadband spectrum photocatalyst based on morphology. *Appl. Surf. Sci.* **368**, 288 (2016).

8. B. Chai, T.Y. Peng, P. Zeng, X.H. Zhang, and X.J. Liu: Template-free hydrothermal synthesis of ZnIn<sub>2</sub>S<sub>4</sub> floriated microsphere as an efficient photocatalyst for H<sub>2</sub> production under visible-light irradiation. *J. Phys. Chem. C* **115**, 6149 (2011).
9. X.L. Xiao, L. Ge, C.C. Han, Y.J. Li, Z. Zhao, X.J. Xin, S.M. Fang, L.N. Wu, and P. Qiu: A facile way to synthesize Ag@AgBr cubic cages with efficient visible-light-induced photocatalytic activity. *Appl. Catal., B* **163**, 564 (2015).
10. Y.P. Bi, S.X. Ouyang, N. Umezawa, J.Y. Cao, and J.H. Ye: Facet effect of single-crystalline Ag<sub>3</sub>PO<sub>4</sub> sub-microcrystals on photocatalytic properties. *J. Am. Chem. Soc.* **133**, 6490 (2011).
11. X.F. Yang, R. Li, Y.Q. Wang, K.Q. Wu, S.F. Chang, and H. Tang: Solvent-induced controllable synthesis of recyclable Ag<sub>2</sub>CO<sub>3</sub> catalysts with enhanced visible light photocatalytic activity. *Ceram. Int.* **42**, 13411 (2016).
12. W. Zhao, Y. Guo, Y. Faiz, W.T. Yuan, C. Sun, S.M. Wang, Y.H. Deng, Y. Zhuang, Y. Li, X.M. Wang, H. He, and S.G. Yang: Facile *in situ* synthesis of Ag/AgVO<sub>3</sub> one-dimensional hybrid nanoribbons with enhanced performance of plasmonic visible-light photocatalysis. *Appl. Catal., B* **163**, 288 (2015).
13. S.W. Cao, J.X. Low, J.G. Yu, and M. Jaroniec: Polymeric photocatalysts based on graphitic carbon nitride. *Adv. Mater.* **27**, 2150 (2015).
14. W.G. Wang, B. Cheng, J.G. Yu, G. Liu, and W.H. Fan: Visible-light photocatalytic activity and deactivation mechanism of Ag<sub>3</sub>PO<sub>4</sub> spherical particles. *Chem.-Asian J.* **7**, 1902 (2012).
15. M.Y. Zhang, L. Li, and X.T. Zhang: One-dimensional Ag<sub>3</sub>PO<sub>4</sub>/TiO<sub>2</sub> heterostructure with enhanced photocatalytic activity for the degradation of 4-nitrophenol. *RSC Adv.* **5**, 29693 (2015).
16. W. Liu, M.L. Wang, C.X. Xu, S.F. Chen, and X.L. Fu: Ag<sub>3</sub>PO<sub>4</sub>/ZnO: An efficient visible-light-sensitized composite with its application in photocatalytic degradation of Rhodamine B. *Mater. Res. Bull.* **48**, 106 (2013).
17. L.L. Zhang, H.C. Zhang, H. Huang, Y. Liu, and Z.H. Kang: Ag<sub>3</sub>PO<sub>4</sub>/SnO<sub>2</sub> semiconductor nanocomposites with enhanced photocatalytic activity and stability. *New J. Chem.* **36**, 1541 (2012).
18. X. Lin, J. Hou, S.S. Jiang, Z. Lin, M. Wang, and G.B. Che: A Z-scheme visible-light-driven Ag/Ag<sub>3</sub>PO<sub>4</sub>/Bi<sub>2</sub>MoO<sub>6</sub> photocatalyst: Synthesis and enhanced photocatalytic activity. *RSC Adv.* **5**, 104815 (2015).
19. G.K. Fu, G.N. Xu, S.P. Chen, L. Lei, and M.L. Zhang: Ag<sub>3</sub>PO<sub>4</sub>/Bi<sub>2</sub>WO<sub>6</sub> hierarchical heterostructures with enhanced visible light photocatalytic activity for the degradation of phenol. *Catal. Commun.* **40**, 120 (2013).
20. H. Xu, H.Z. Zhao, Y.G. Xu, Z.G. Chen, L.Y. Huang, Y.P. Li, Y.H. Song, Q. Zhang, and H.M. Li: Three-dimensionally ordered macroporous WO<sub>3</sub> modified Ag<sub>3</sub>PO<sub>4</sub> with enhanced visible light photocatalytic performance. *Ceram. Int.* **42**, 1392 (2016).
21. L. Liu, Y.H. Qi, J.R. Lu, S.L. Lin, W.J. An, Y.H. Liang, and W.Q. Cui: A stable Ag<sub>3</sub>PO<sub>4</sub>@g-C<sub>3</sub>N<sub>4</sub> hybrid core@shell composite with enhanced visible light photocatalytic degradation. *Appl. Catal., B* **183**, 133 (2016).
22. X.M. Qi, M.L. Gu, X.Y. Zhu, J. Wu, Q. Wu, H.M. Long, and K. He: Controlled synthesis of Ag<sub>3</sub>PO<sub>4</sub>/BiVO<sub>4</sub> composites with enhanced visible-light photocatalytic performance for the degradation of RhB and 2,4-DCP. *Mater. Res. Bull.* **80**, 215 (2016).
23. L.W. Lei, H.H. Jin, Q. Zhang, J. Xu, D. Gao, and Z.Y. Fu: A novel enhanced visible-light-driven photocatalyst via hybridization of nanosized BiOCl and graphitic C<sub>3</sub>N<sub>4</sub>. *Dalton Trans.* **44**, 795 (2015).
24. Q.Z. Teng, X.S. Zhou, B. Jin, J. Luo, X.Y. Xu, H.J. Guan, W. Wang, and F. Yang: Synthesis and enhanced photocatalytic activity of a BiO/TiO<sub>2</sub> nanobelt array for methyl orange degradation under visible light irradiation. *RSC Adv.* **6**, 36881 (2016).
25. Y.H. Xiang, P. Ju, Y. Wang, Y. Sun, D. Zhang, and J.Q. Yu: Chemical etching preparation of the Bi<sub>2</sub>WO<sub>6</sub>/BiOI p-n heterojunction with enhanced photocatalytic antifouling activity under visible light irradiation. *Chem. Eng. J.* **288**, 264 (2016).
26. L. Kong, Z. Jiang, T.C. Xiao, L.F. Lu, M.O. Jones, and P.P. Edwards: Exceptional visible-light-driven photocatalytic activity over BiOBr-ZnFe<sub>2</sub>O<sub>4</sub> heterojunctions. *Chem. Commun.* **47**, 5512 (2011).
27. J.X. Xia, J. Di, S. Yin, H. Xu, J. Zhang, Y.G. Xu, L. Xu, H.M. Li, and M.X. Ji: Facile fabrication of the visible-light-driven Bi<sub>2</sub>WO<sub>6</sub>/BiOBr composite with enhanced photocatalytic activity. *RSC Adv.* **4**, 82 (2014).
28. W.B. Li, Y.P. Zhang, Y.Y. Bu, and Z.Y. Chen: One-pot synthesis of the BiVO<sub>4</sub>/BiOBr heterojunction composite for enhanced photocatalytic performance. *J. Alloys Compd.* **680**, 677 (2016).
29. Y.C. Miao, H.B. Yin, L. Peng, Y.N. Huo, and H.X. Li: BiOBr/Bi<sub>2</sub>MoO<sub>6</sub> composite in flower-like microspheres with enhanced photocatalytic activity under visible-light irradiation. *RSC Adv.* **6**, 13498 (2016).
30. Y.J. Sun, W.D. Zhang, T. Xiong, Z.W. Zhao, F. Dong, R.Q. Wang, and W.K. Ho: Growth of BiOBr nanosheets on C<sub>3</sub>N<sub>4</sub> nanosheets to construct two-dimensional nanojunctions with enhanced photoreactivity for NO removal. *J. Colloid Interface Sci.* **418**, 317 (2014).
31. B.C. Cao, P.Y. Dong, S. Cao, and Y.H. Wang: BiOCl/Ag<sub>3</sub>PO<sub>4</sub> composites with highly enhanced ultraviolet and visible light photocatalytic performances. *J. Am. Ceram. Soc.* **96**, 544 (2013).
32. O. Mehraj, N.A. Mir, B.M. Pirzada, and S. Sabir: Fabrication of novel Ag<sub>3</sub>PO<sub>4</sub>/BiOBr heterojunction with high stability and enhanced visible-light-driven photocatalytic activity. *Appl. Surf. Sci.* **332**, 419 (2015).
33. Y.Q. Wang, X.F. Cheng, X.T. Meng, H.W. Feng, S.G. Yang, and C. Sun: Preparation and characterization of Ag<sub>3</sub>PO<sub>4</sub>/BiOI heterostructure photocatalyst with highly visible-light-induced photocatalytic properties. *J. Alloys Compd.* **632**, 445 (2015).
34. Z.K. Cui, M.M. Si, Z. Zheng, L.W. Mi, W.J. Fa, and H.M. Jia: Preparation and characterization of Ag<sub>3</sub>PO<sub>4</sub>/BiOI composites with enhanced visible light driven photocatalytic performance. *Catal. Commun.* **42**, 121 (2013).
35. Z. Jiang, F. Yang, G.D. Yang, L. Kong, M.O. Jones, T.C. Xiao, and P.P. Edwards: The hydrothermal synthesis of BiOBr flakes for visible-light-responsive photocatalytic degradation of methyl orange. *J. Photochem. Photobiol., A* **212**, 8 (2010).
36. Y.N. Huo, J. Zhang, M. Miao, and Y. Jin: Solvothermal synthesis of flower-like BiOBr microspheres with highly visible-light photocatalytic performances. *Appl. Catal., B* **111**, 334 (2012).
37. D. Zhang, J. Li, Q.G. Wang, and Q.S. Wu: High {001} facets dominated BiOBr lamellas: Facile hydrolysis preparation and selective visible-light photocatalytic activity. *J. Mater. Chem. A* **1**, 8622 (2013).
38. Z.G. Xiong, L.L. Zhang, J.Z. Ma, and X.S. Zhao: Photocatalytic degradation of dyes over grapheme-gold nanocomposites under visible light irradiation. *Chem. Commun.* **46**, 6099 (2010).